Journal of Astronomical Telescopes, Instruments, and Systems

AstronomicalTelescopes.SPIEDigitalLibrary.org

Design of a broadband soft x-ray polarimeter

Herman L. Marshall
H. Moritz Günther
Ralf K. Heilmann
Norbert S. Schulz
Mark Egan
Tim Hellickson
Sarah N. T. Heine
David L. Windt
Eric M. Gullikson
Brian Ramsey
Gianpiero Tagliaferri
Giovanni Pareschi

SPIE.

Herman L. Marshall, H. Moritz Günther, Ralf K. Heilmann, Norbert S. Schulz, Mark Egan, Tim Hellickson, Sarah N. T. Heine, David L. Windt, Eric M. Gullikson, Brian Ramsey, Gianpiero Tagliaferri, Giovanni Pareschi, "Design of a broadband soft x-ray polarimeter," *J. Astron. Telesc. Instrum. Syst.* **4**(1), 011005 (2018), doi: 10.1117/1.JATIS.4.1.011005.

Design of a broadband soft x-ray polarimeter

Herman L. Marshall,[a,*] H. Moritz Günther,[a] Ralf K. Heilmann,[a] Norbert S. Schulz,[a] Mark Egan,[a] Tim Hellickson,[a,b] Sarah N. T. Heine,[a] David L. Windt,[c] Eric M. Gullikson,[d] Brian Ramsey,[e] Gianpiero Tagliaferri,[f] and Giovanni Pareschi[f]
[a]MIT Kavli Institute, Cambridge, Massachusetts, United States
[b]Colorado University, Laboratory of Atmosphere and Space Physics, Boulder, Colorado, United States
[c]Reflective X-ray Optics, New York, New York, United States
[d]Lawrence Berkeley National Laboratory, Berkeley, California, United States
[e]NASA Marshall Space Flight Center, Huntsville, Alabama, United States
[f]Istituto Nazionale di Astrofisica, Osservatorio Astronomico di Brera, Milano, Italy

Abstract. We describe an optical design and possible implementation of a broadband soft x-ray polarimeter. Our arrangement of gratings is designed optimally for the purpose of polarimetry with broadband focusing optics by matching the dispersion of the spectrometer channels to laterally graded multilayers (LGMLs). The system can achieve polarization modulation factors over 90%. We implement this design using a single optical system by dividing the entrance aperture into six sectors; high efficiency, blazed gratings from opposite sectors are oriented to disperse to a common LGML forming three channels covering the wavelength range from 35 to 75 Å (165 to 350 eV). The grating dispersions and LGML position angles for each channel are 120 deg to each other. CCD detectors then measure the intensities of the dispersed spectra after reflection and polarizing by the LGMLs, giving the three Stokes parameters needed to determine a source's linear polarization fraction and orientation. The design can be extended to higher energies as LGMLs are developed further. We describe examples of the potential scientific return from instruments based on this design. [DOI: 10.1117/1.JATIS.4.1.011005]

Keywords: x-ray; polarimeter; astronomy; multilayer; mirror; grating.

Paper 17097SSP received Nov. 23, 2017; accepted for publication Mar. 12, 2018; published online Apr. 6, 2018.

1 Introduction

Over 40 years, the x-ray polarization of only the crab nebula has been measured to better than 3σ, as found using OSO-8.[1,2] Over the entire history of x-ray astronomy, there has never been a mission or instrument flown that was designed to measure the polarization of x-rays below 1 keV. We have developed a design that should be able to measure x-ray polarization over a broad energy range of x-rays below 1 keV.

The value of x-ray polarimetry to the scientific community was underscored by NASA's selection of the Imaging X-ray Polarimetry Explorer (IXPE[3]), in the most recent NASA SMEX cycle. IXPE uses photoelectron-tracking detectors with sensitivity in the 2- to 8-keV band. Our design provides a broadband capability below 1 keV that is complementary to IXPE and other instruments operating at higher energies. Although fundamentally based on Bragg reflection, our design mitigates the intrinsically narrow band nature of such reflectors. See Kaaret[4] for a general discussion of polarimeters based on Bragg reflection (e.g., OSO-8), those based on photoelectron tracking (e.g., IXPE), and those based on Compton scattering (e.g., PoGO+[5]). Some sources, such as many isolated neutron stars (NSs), are predominantly observable only below 1 keV, where the effects of vacuum birefringence can be observed. It is likely that the polarization fraction or position angle vary with energy in many astrophysical situations (see Sec. 5), addressable using an instrument of our design in combination with IXPE. For example, there could be a polarization angle swing of 90 deg in AGN spectra near 2 keV due to return radiation.[6]

We have presented early designs in various proceedings,[7–10] but in this paper, we provide a fundamental optical design developed specifically for use in a soft x-ray polarimeter. In Sec. 2, we present the basic design, whereas Sec. 3 provides details of an implementation that can detect polarizations of various sources even in exposures of a few hundred seconds as are available in a sounding rocket experiment (the rocket experiment demonstration of a soft x-ray polarimeter, or the REDSoX Polarimeter). (The name of the instrument is used with the permission of Major League Baseball and the Red Sox Baseball Club.) The implementation is based on the demonstrated performances of previously fabricated components and could be readily adapted for an orbital mission. In Sec. 4, we present ray-tracing results to validate the basic design and assess the fabrication and operational tolerances. In Sec. 5, we describe observations that could be carried out with a sounding rocket experiment and the scientific return from an orbital version of the instrument.

2 Optical Design

2.1 *Overview*

Our design starts with a dispersive x-ray spectrometer using gratings. Figure 1 shows a single-channel schematic design, with focusing optical assembly ("mirror"), gratings placed at some location along the optical axis, a multilayer (ML)-coated flat at the focus of the spectrometer thus created, and a detector for the reflected spectra. Figure 2 shows a rendered three-dimensional (3-D) view of all optical elements, with three independent

*Address all correspondence to: Herman L. Marshall, E-mail: hermanm@space.mit.edu

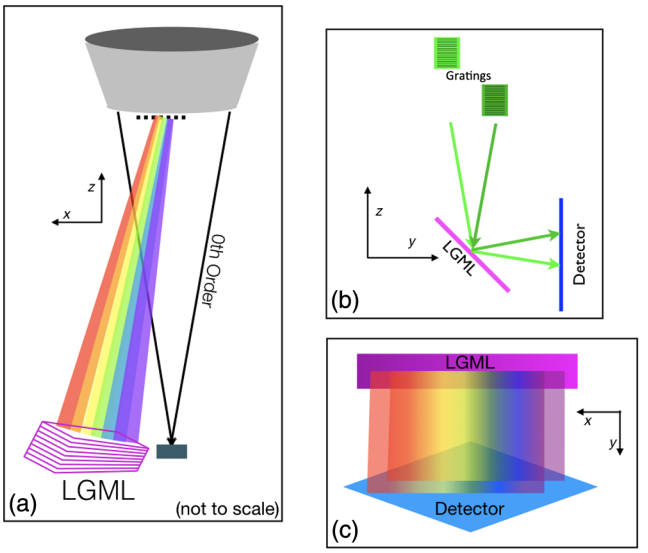

Fig. 1 A schematic layout of a soft x-ray polarimeter. (Note, some dimensions and orientations are exaggerated for illustration.) (a) Overview of the optical elements with a focusing mirror at top, a transmission grating in the converging beam, an LGML coated flat at the spectroscopic focus, and an imaging detector at the prime focus (where zeroth order is observed). The gratings act like a prism, dispersing x-rays with short wavelengths closest to zeroth order and incident on the LGML at the small layer spacing end, whereas long wavelengths disperse farther from zeroth order, where the LGML period is largest. The optical axis is along the z-coordinate. Only one channel is shown here, which disperses along the x-axis. (b) Gratings on either side of the optical axis disperse the spectrum to a line in the focal plane (defining $z = 0$) along the x-axis. Rays from gratings placed at different distances along z have different incidence angles at the LGML and reflect to different z values at the detector. (c) Approximate view from the point of view of the focusing optics. The LGML is shaded to indicate a changing period along its surface. Different sides of the telescope aperture disperse to different locations on the LGML, coinciding at the focal surface ($z = 0$), along the center line of the LGML, and then reflecting to different locations on the detector (tilted slightly in this view).

channels and many grating facets for each channel. To have only one mirror but be able to measure at least three independent position angles and, consequently, three Stokes parameters, we subdivide the entrance aperture into six sectors at 60 deg apart. Using blazed gratings, where most power goes into $+1$ order, we align opposing sectors so that these focus to the same ML flat. There are then three spectroscopy channels, with an ML flat and a detector each. Finally, the period of the ML coating is laterally graded to match the Bragg peak of the ML reflectivity with the dispersion of the gratings.

For an x-ray spectrometer designed to optimize spectral resolution along a single dispersion line in the focal plane, transmission gratings are usually arranged in a faceted Rowland configuration (A good example of an x-ray spectrometer in the Rowland configuration[11] is the High-Energy Transmission Grating Spectrometer[12] on the "Chandra" x-ray observatory.), with gratings tangent to a torus whose major and minor diameters are half of the distance from the grating assembly to the telescope's focal surface. The basic design of our polarimeter involves matching the near-linear dispersion of the gratings to the lateral grading of a ML-coated flat set at about 45 deg to the incoming light. In the x-ray band, this orientation nulls the reflectivity of the polarization in the plane of the reflection (the s polarization); at the Brewster angle (very close to 45 deg for x-rays) the reflected light is 100% polarized with the electric vector perpendicular to the reflection plane (the p polarization). CCD detectors view each ML to determine the intensity reflected from that ML.

By orienting three ML-coated flats at position angles 120 deg apart, we can measure the three Stokes parameters I, Q, and U at any time without instrument rotation. Each channel measures a specific combination of I, Q, and U; arranging three flats to be oriented at 120 deg from each other provides optimal independence among the measurements so that the three Stokes parameters can be determined. The fraction of linearly polarized light is given by $\Pi = \sqrt{Q^2 + U^2}/I$. The sensitivity of an x-ray polarimeter is often characterized by the minimum detectable polarization (MDP) that can be achieved for a given source, as discussed in Sec. 3.6. The zeroth-order CCD detector can also be used to determine I, providing some redundancy. See Sec. 3.6 and particularly Eq. (18) for details about how to compute the Stokes parameters from the observations.

To get an approximate, intuitive feel for a workable design, we begin with a simplistic model, where gratings are placed in the converging beam of a focusing mirror with focal length F. We constrain the design for simplicity of fabrication to require using gratings with all the same period, P. Furthermore, the system must focus x-rays of a given wavelength, λ, to a relatively small region on the ML, where the Bragg condition is satisfied, resulting in placing the ML-coated flat (not the detector) at the spectroscopic focus of the system. We define a coordinate system where z is oriented along the optical axis, with $z = 0$ at the on-axis focus and the $+z$-direction is oriented toward the mirror. A transmission grating is placed at location $(0, y, z)$, with its normal along the direction to the telescope focus at (0,0,0) but dispersing x-rays to positions $(x, 0, 0)$. The dispersion of the grating is given by the grating equation $m\lambda = P \sin\alpha$, where m is the grating order of interest (which we take to be $+1$) and α is the dispersion angle. For small angles, $\alpha \approx x/z$. Our goal is to match the dispersed wavelength to the peak reflectivity of a laterally graded multilayer (LGML), for which the Bragg condition is given by $\lambda = 2D \cos\theta$, where D is the ML period and θ is the angle of incidence relative to the LGML normal; $\theta \approx y/z + \pi/4$, for a ML-coated flat that is placed at 45 deg to the optical axis. For a linear period gradation, $D = Gx$, where x is the distance along the LGML. Again, the simplest design is when G is the same for all LGMLs.

We match the LGML's Bragg peak to the grating dispersion by setting $P \sin\alpha \approx Px/z = 2D \cos\theta = 2Gx \cos\theta$, giving $z = P/(2G \cos\theta)$, so $z = P/(2G \cos[y/z + \pi/4])$. Thus, gratings are shifted along the z-axis as the grating is displaced away from the optical axis along the y-axis. Because y/z is usually small compared with $\pi/4$, z varies with y nearly linearly. Next, we provide a rigorous derivation of how to place gratings in our design.

2.2 *Grating Positioning*

Determining the positions of the gratings is the key to our design. Here, we provide a rigorous derivation of the requirements for a multigrating design. In what follows, we use two approximations: $P \gg \lambda$ and $\alpha \ll 1$. For the implementation discussed in Sec. 3, $P = 2000$ Å while $\lambda < 75$ Å, so $\lambda/P < 0.04$. The maximum value of α is dictated by realistic x-ray optics for broadband use with two reflections, so $\alpha = 4\alpha_g$, where α_g is the graze angle for total internal reflection that yields reflectivities

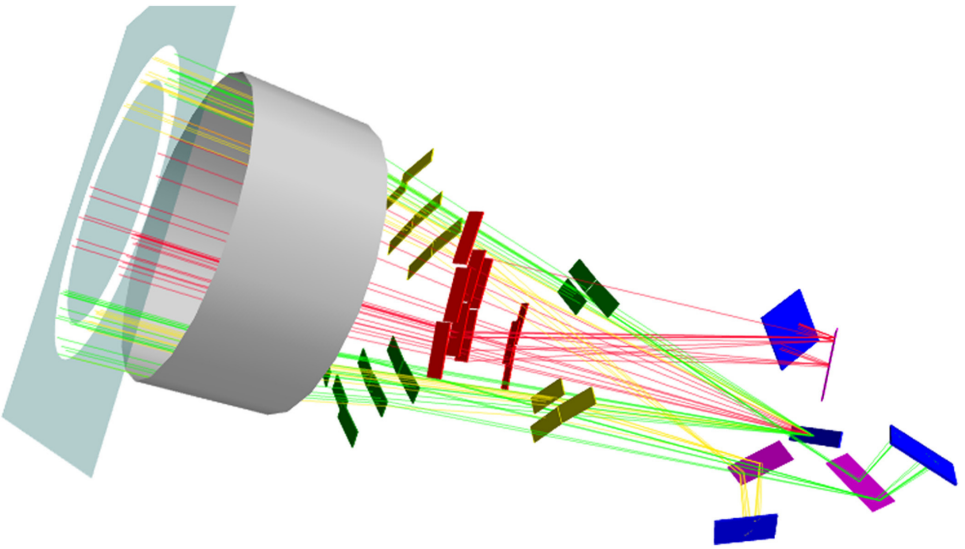

Fig. 2 Raytrace-based schematic of the soft x-ray polarimeter design, as in the REDSoX polarimeter. In this sketch, the total length of the instrument is shortened relative to the mirror diameter to improve clarity. Photons enter through the annular aperture and are focused by the optics assembly made from concentric shells (gray cylinder). Gratings are arranged in three channels (shown in green, red, and yellow) comprising opposing 60-deg azimuthal sectors within the annular aperture. Monochromatic rays are colored according to the channel. The zeroth-order photons pass through the gratings to the central detector (blue). Others are diffracted and land on one of the three polarizing LGMLs (magenta), which reflect them onto that channel's detector (blue). Viewers can interact with this figure in the Supplemental Content using Adobe Acrobat. (3D Multimedia 1, PDF, 5.66 MB) [URL: http://dx.doi.org/10.1117/1.JATIS.4.1.011005.1].

above 90%. For our proposed implementation, $\alpha_g < 1.3$ deg, so $\alpha < 0.1$ rad. Both approximations are justified *post facto* as the design is verified by ray tracing, as shown in Sec. 4.

First order from the grating will fulfill the local Bragg condition depending on the angle between the ray and LGML normal $\overrightarrow{n_m}$. Photons pass through the mirror and are focused toward (0,0,0). We choose the $+x$-axis of the coordinate system as the dispersion direction. The $+x$-axis is also chosen to be in the plane of the LGML, whose unit normal pointing toward the reflective surface is

$$\overrightarrow{n_m} = -\frac{1}{\sqrt{2}}\begin{pmatrix}0\\1\\1\end{pmatrix}. \tag{1}$$

The ML coating is laterally graded, i.e., the period depends on the x-coordinate

$$D(x) = G_0 + xG, \tag{2}$$

where G_0 is the (extrapolated) period of the ML at $x = 0$. We assume $G = 0.88$ Å mm^{-1} for the basic design, based on prototype LGMLs (see Sec. 3). The Bragg condition at position x then requires

$$n\lambda = 2D(x)|\vec{X} \cdot \overrightarrow{n_m}|, \tag{3}$$

where the ray's direction vector is $\vec{X}$. We design the system to work with the first-order Bragg peak, $n = 1$, which gives the best ML reflectivity and matches the high efficiency in first order for critical angle transmission (CAT) gratings (see Sec. 3). Using only first order for both the LGML Bragg peaks and the CAT gratings also minimizes the length of the dispersion for a given wavelength range in the dispersed spectrum.

2.2.1 *Gratings on the optical axis*

We examine the special case of a grating that is located on the optical axis at the coordinates $(0, 0, z_g)$. The grating equation is

$$\sin\alpha = m\frac{\lambda}{P}, \tag{4}$$

for diffraction into order m. We will design the instrument to work with photons in diffraction order $m = +1$. The propagation direction of first-order photons leaving the grating is

$$\vec{X} = \begin{pmatrix}\sin\alpha\\0\\-\cos\alpha\end{pmatrix}. \tag{5}$$

Photons are going to hit the LGML at

$$x = z_g \tan(\alpha). \tag{6}$$

Combining the previous three equations with the Bragg condition in Eq. (3) and using a small angle approximation for α with $\cos\alpha \approx 1$ and $\tan\alpha \approx \sin\alpha$, we can solve for the best grating position z_g

$$z_g = \frac{P}{\sqrt{2}G} - \frac{PG_0}{G\lambda}. \tag{7}$$

From this equation, we can see that z_g will depend on wavelength λ unless $G_0 = 0$. This wavelength dependence is not a desirable property for this design and would also hold for gratings that are not on the optical axis. Therefore, we require $G_0 = 0$ in Eq. (2) for the remainder of this paper.

2.2.2 *General grating positioning*

We now introduce a spherical coordinate system as shown in Fig. 3. The polar angle (γ_g) is measured with respect to the x-axis and the yz-plane is the equatorial plane. This frame is more convenient than the usual definition, where the polar angle is measured with respect to the z-axis because x is the direction along which the period of the ML flat changes. Consider a grating located at

$$\overrightarrow{X_g} = r_g \begin{pmatrix} \cos\gamma_g \\ \sin\gamma_g \sin\beta_g \\ \sin\gamma_g \cos\beta_g \end{pmatrix}, \tag{8}$$

where r_g is the distance between the grating and the focal point (located at the origin of the coordinate system), γ_g is the polar angle, and β_g is the azimuthal angle measured in the yz-plane from the z-axis. These angles are shown in Fig. 3. A photon incident upon this grating will have the direction vector $\vec{X} = -(\sin\gamma_g, \cos\gamma_g \sin\beta_g, \cos\gamma_g \cos\beta_g)$. We place the gratings so that they are essentially perpendicular to the incoming photons (except for an adjustment for the blaze angle described in Sec. 2.5) to reduce the shadows cast by the grating support structure (see Sec. 3). We also want to orient the gratings such that they disperse along the x-axis. We can then write the diffraction of photons as a rotation with angle α from Eq. (4) around the axis $\vec{A}$

$$\vec{A} = \overrightarrow{X_g} \times \begin{pmatrix} 1 \\ 0 \\ 0 \end{pmatrix} = \begin{pmatrix} 0 \\ \sin\gamma_g \cos\beta_g \\ -\sin\gamma_g \sin\beta_g \end{pmatrix}. \tag{9}$$

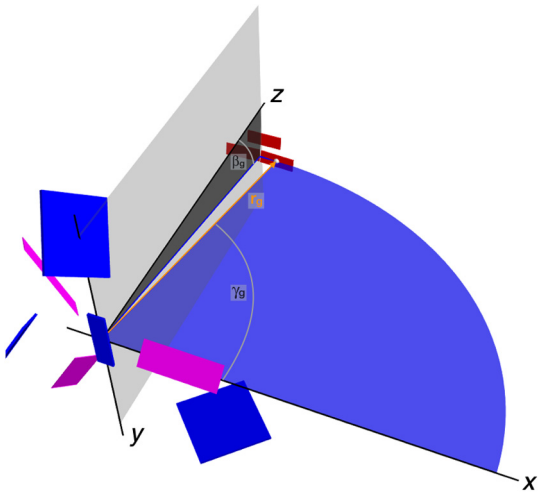

Fig. 3 Sketch of the geometry, showing three polarimetry channel detectors (blue), one direct imaging detector (blue rectangle at the coordinate system origin), three ML flats (magenta rectangles), and three gratings (red rectangles). The distance r_g (orange vector) is from the origin to the center of the grating marked by the gray point. The angle γ_g, indicated by the blue wedge, is the angle to the grating from the x-axis. The angle β_g, indicated by the dark gray wedge, is the angle between the z-axis and the projection of the line to the grating center onto the yz-plane.

We can write the rotation matrix around this axis as

$$\begin{aligned} R = \cos\alpha \mathsf{E} &+ \sin\alpha \begin{pmatrix} 0 & \sin\gamma_g \sin\beta_g & \sin\gamma_g \cos\beta_g \\ -\sin\gamma_g \sin\beta_g & 0 & 0 \\ -\sin\gamma_g \cos\beta_g & 0 & 0 \end{pmatrix} \\ &+ (1-\cos\alpha) \begin{pmatrix} 0 & 0 & 0 \\ 0 & \dots & \dots \\ 0 & \dots & \dots \end{pmatrix}, \end{aligned} \tag{10}$$

where E is the identity matrix and we use the approximation $\cos(\alpha_g) \approx 1$. The direction vector $\overrightarrow{X_1}$ of a dispersed first-order photon is

$$\begin{aligned} \overrightarrow{X_1} &= R\vec{X} \\ &= -\begin{pmatrix} \sin\gamma_g \\ \cos\gamma_g \sin\beta_g \\ \cos\gamma_g \cos\beta_g \end{pmatrix} - \frac{\lambda}{P} \begin{pmatrix} \cos^2\gamma_g \\ -\sin\gamma_g \cos\gamma_g \sin\beta_g \\ -\sin\gamma_g \cos\gamma_g \cos\beta_g \end{pmatrix}, \end{aligned} \tag{11}$$

where we have used Eq. (4).

We can now plug this photon direction vector into the Bragg condition, Eq. (3), use Eq. (2), and set $G_0 = 0$ to obtain

$$\lambda = \sqrt{2}Gx \cos\gamma_g (\sin\beta_g + \cos\beta_g)\left(1 - \frac{\lambda}{P}\sin\gamma_g\right), \tag{12}$$

where the last term can be dropped because the wavelength λ is much smaller than the grating constant P in our implementation.

We need to express the position x in terms of the grating coordinates and the photon wavelength λ. The equation for a diffracted ray is

$$\vec{X}' = \overrightarrow{X_g} + c\overrightarrow{X_1}, \tag{13}$$

for some value of c. It is sufficient to just write out the z-component of this equation to see where the ray intersects the LGML, which will happen when the ray passes the plane $z = 0$. Solving for c gives

$$c = \frac{r_g P}{P - \lambda \sin\gamma_g} \approx r_g, \tag{14}$$

and substituting this result into the x-component of Eq. (13) yields

$$x = \frac{r_g}{P}\lambda \sin^2\gamma_g. \tag{15}$$

Last, we obtain r_g for a grating for any given γ_g, β_g by inserting Eq. (15) into Eq. (12)

$$r_g = \frac{P}{\sqrt{2}G \sin^3\gamma_g (\sin\beta_g + \cos\beta_g)}. \tag{16}$$

With Eq. (16), we then have the position of the grating using Eq. (8) given values of γ_g and β_g.

2.3 *Filling the Space Available With Gratings*

Equation 16 specifies where a grating must be positioned for a given (γ_g, β_g) to direct photons with $m = +1$ to the LGML so that the Bragg condition is satisfied. The transmission gratings planned for our implementation of the design have finite size and should be placed normal to the incoming (converging) photons. For these reasons, the gratings cannot follow the shape of the surface given by Eq. (16) exactly but can be approximated sufficiently. In our implementation, we place gratings in a rectangular grid to fill the annulus under the mirror shells that is traversed by the photons after focusing. We apply Eq. (16) to the center of each grating and use ray-tracing to calculate the nonideal effects arising from the finite size of flat gratings.

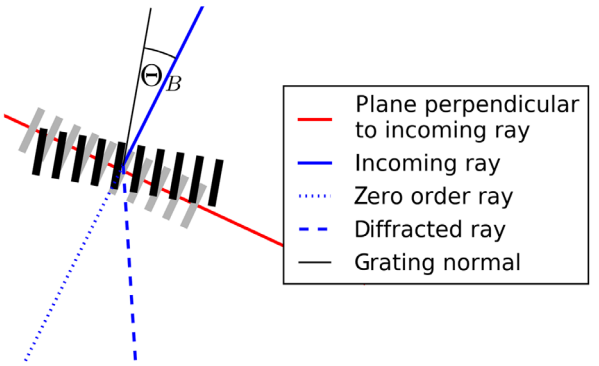

Fig. 4 Sketch of a critical angle transmission (CAT) grating. The solid blue line is the path of the incoming photon. The red line is perpendicular to the incoming photon and would be the plane of a traditional transmission grating (gray grating bars). Instead, the CAT grating is blazed by the angle Θ_B, which makes photons "bounce off" the walls of the grating bars (thick black lines) and all the dispersed signal ends up toward the right of the zeroth order. Instead, the blaze angle was $-\Theta_B$, photons would "bounce off" the other side of the grating bars and would be blazed toward a location to the left of the zeroth order. Note that for the blaze angle Θ_B the angle between the incoming ray (solid blue line) and the diffracted ray (dashed blue line) is $2\Theta_B$. Sometimes this $2\Theta_B$ angle is called "blaze angle" in the literature, which can lead to confusion.

The result for our sounding rocket implementation can be seen in Sec. 3.2.

2.4 *Multiple Channels*

As described in Secs. 1 and 2.1, the REDSoX polarimeter consists of three LGMLs and corresponding detectors that measure polarization independently. To achieve this, the rectangular grid of gratings does not cover the full annulus but only two opposing sectors, each of which is 60-deg wide. An opposing pair of sector images onto one of the LGMLs; the combination of gratings, LGML, and detector comprises a "channel." One of the two segments in each channel is "high" [larger r_g because $\beta > 0$, see Eq. (16)], and the other one is "low" (smaller r_g because $\beta < 0$).

There are three channels. For channels 2 and 3, all gratings and the corresponding LGML and CCD detector are rotated by 120 deg and -120 deg, respectively, around the optical axis with respect to channel 1. See Figs. 2, 8, and 13.

2.5 *Grating Blaze Angle*

The grating placement as discussed above is for transmission gratings with similar efficiencies in positive and negative diffraction orders. To reduce mass and cost, we plan to use gratings in which the diffraction efficiency is maximized to one side by blazing (tilting) the grating surface. To take advantage of the blaze feature, every grating is rotated by θ_B around the grating bar axis, which we will define as its pitch (Fig. 4). Generally, θ_B is small enough that there is no significant shadowing by the grating support structure.

3 Implementation

Our optical schematic has been proposed to NASA for implementation in a sounding rocket configuration. This implementation was dubbed the rocket experiment demonstration of a soft x-ray polarimeter or the REDSoX polarimeter. The main constraints on a sounding rocket payload are the maximum diameter of the optics assembly, about 0.45 m, and the total length of the instrument, limiting the mirror's focal length to 2.5 m. Exposure

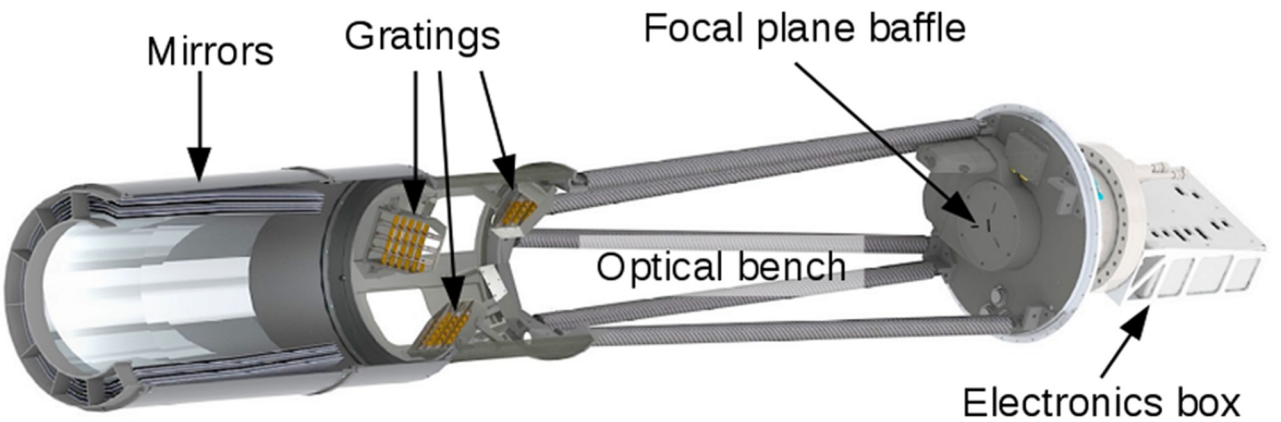

Fig. 5 Cutaway rendering of the REDSoX polarimeter from an engineering design, showing the mirror, gratings (in gold), the optical bench, the focal plane baffle (with three slits for dispersed events) over the pendulum valve for the detector chamber, and the back of the detector chamber with the electronics box. The top and bottom grating groups intercept opposite 60-deg sectors of focused x-rays, dispersing them through the baffle slit to the left of the central (rectangular) aperture for zeroth order. See Fig. 13 for a rendering of the interior of the detector chamber. For clarity, only a few mirror shells and grating groups are rendered.

time is limited by the total mass of the payload, which includes the attitude system. For the REDSoX polarimeter, this exposure time is about 300 s. We now describe the components of the REDSoX polarimeter as currently designed; more details can be found elsewhere.[13] Figure 5 shows a rendering of our implementation.

3.1 *Focusing Optics*

The broadband focusing mirror should work well in the energy range appropriate to the available MLs that can be used in the 0.1- to 1.0-keV range. Type I Wolter designs are effective here, so we define the inner and outer radii as r_I and r_O. The telescope's f-ratio should not be very small; the sounding rocket constraints provide an f-ratio over 5, which suffices. The requirement on the mirror half-power diameter (HPD) will be determined by setting a limit on the spectrometer's spectral resolution, which is derived from the gradient, G, of the laterally graded ML (see Sec. 3.3). We anticipate that HPDs of $<30''$ will be sufficient and have been demonstrated by researchers at the Brera Observatory[14,15] and at the Marshall Space Flight Center.[16] Five mandrels were made for the Micro-X project[17] with a 2500-mm focal length, so we adopt this focal length. The focal plane scale is $82''/\text{mm}$.

For the REDSoX polarimeter, there would be nine shells, with inner radii ranging from 14.96 to 20.22 cm and outer radii ranging from 16.94 to 22.88 cm. The mirror geometric area is about 640 cm^2, and we assume that the support structure blocks 12% of this area and then use reflectivity given by two reflections from Ni-coated surfaces using the known graze angles. The total mass of the mirror is expected to be about 78 kg.

3.2 *Gratings*

For gratings, we baseline critical angle transmission (CAT) gratings[18] developed in the Space Nanotechnology Lab (SNL) at MIT. These can now be reliably produced in a 10×30 mm (and a 30×30) format with period $P = 2000$ Å on 0.5-mm-thick Si wafer substrates.[19,20] We extrapolated measurements taken at the advanced light source (ALS) to 70 Å using an efficiency model and then accounted for structural obscuration to generate an efficiency model for our baseline effective area. We further note that the measured efficiencies in the 30- to 70-Å range are generally closer to the models than the measurements below 30 Å.[21]

Fig. 6 Engineering drawing of a CAT grating in a holder. The L2 support structure is visible as the hexagonal structure that is 0.5-mm deep; the grating is a 4-μm layer on top, with the dispersion along the long axis.

A grating in a holder is shown schematically in Fig. 6 and several gratings are assembled stair-stepped into one "sector" as shown in Fig. 7. The sectors are mounted approximately azimuthally about the optical axis, as shown in Fig. 8, so that the dispersion direction is along the long dimension. The gratings are mounted in a blazed configuration, rotated so that x-rays reflect off of the polished grating sidewalls, increasing the efficiency in (what we define as) positive orders. The blaze condition is described in Sec. 2.5 and shown in Fig. 4. The system MDP (from Sec. 3.6) varies inversely with the square root of the grating efficiency, so we computed the MDP as a function of

Fig. 7 Engineering design of an assembly of gratings for one (high) sector of the REDSoX polarimeter. The gratings are aligned to disperse either to the left or to the right, depending on whether the assembly is high or low along the optical axis. The gratings are stair-stepped so that the Bragg condition is met at the ML. Ribs have pins to securely position gratings below the Invar mounts and flexible arms above to maintain location.

Fig. 8 Grating assemblies as installed on the optical bench of the REDSoX polarimeter.

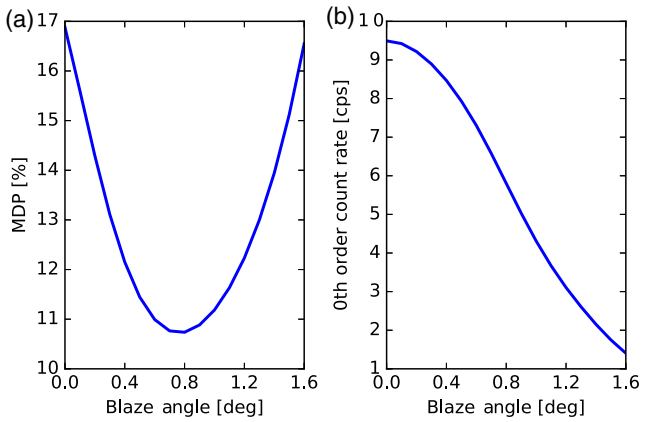

Fig. 9 For the example of Mk 421, this shows the calculation of (a) the MDP and (b) zeroth-order count rate as a function of the CAT grating blaze angle in the REDSoX polarimeter implementation. At 0.8 deg, the MDP is optimized at the expense of the count rate in the zeroth order. The MDP is insensitive to the blaze angle within 0.15 deg of the optimum, setting the mounting angle tolerance.

blaze angle, finding a minimum at about 0.8 deg (see Fig. 9). To increase the efficiency for dispersed x-rays, the throughput in the zeroth order is decreased, as shown in Fig. 9.

3.3 *Laterally Graded Multilayer Coatings*

Under NASA funding, there is demonstrated performance of LGMLs coated flats. An image of such an LGML is shown in Fig. 10. LGMLs have been made by reflective x-ray optics (RXO) and the center for x-ray optics (CXRO) that are suitable for our design. The coating substrates are portions of highly polished Si wafers, about 0.5-mm thick. They have linear period spacing gradients of 0.88 Å/mm to reflect and polarize x-rays from 17 to 75 Å (165 to 730 eV). The coating material pairs were W/B_4C, C/CrCo, $Cr/B_4C/Sc$, and La/B_4C. Reflection efficiencies at 45 deg were measured at the ALS in Berkeley, California, at 1- or 2-mm spacing for each LGML.[9,10] Results of these tests are shown in Fig. 11 for the

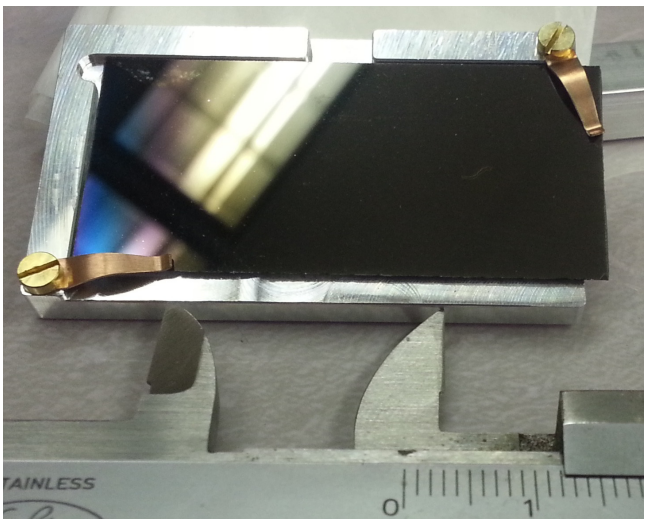

Fig. 10 A LGML coated flat from RXO in a lab holder. It is about 0.5-mm thick and 47-mm long. The ML period, *d*, increases from left to right.

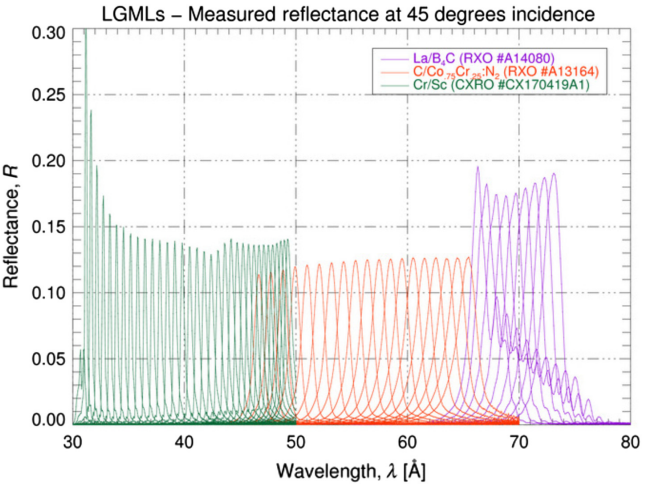

Fig. 11 Reflectivity measurements of LGMLs[9,10] using a partially polarized beam at the ALS in Berkeley. The reflectivities were sampled at 1-mm spacing, starting below 30 Å (about 0.4 keV) for the Cr/Sc sample (green) and at 2-mm spacing for the C/CoCr (red) and La/B_4C (violet) samples.

wavelength range of interest. Across each LGML, the Bragg peak deviates from linearity by <1%, ×2 smaller than the FWHM of the peak (Fig. 12).

The reflectivities of the LGMLs are critical to the performance of this design. The baseline implementation selects the 35 to 75 Å wavelength range due to the extents of the CCD detectors and the spectrometer dispersion relation. Referring to Fig. 11, the Cr/Sc LGML has the best reflectivity in the 35 to 50 Å range, C/CrCo is best in the 40 to 67 Å range, and La/B_4C is best longward of 67 Å. The flight LGML will be a mosaic of the three types, cut precisely at positions corresponding to Bragg peaks at 50 and/or 67 Å depending on the LGML and mounted as an assembly for flight. The LGML assemblies will be the same for each channel. When corrected for the ALS beam polarization, the average reflectivity to unpolarized light is about 10%.

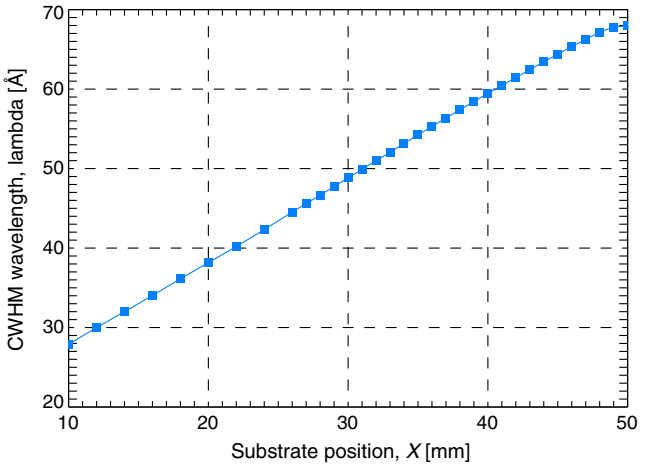

Fig. 12 Bragg peak wavelength as a function of position along a LGML (A13164), made from alternating layers of C and a CoCr alloy. The centroid of the Bragg peak is linear with position along the LGML to better than 1%, sufficient for an instrument, such as the REDSoX polarimeter.

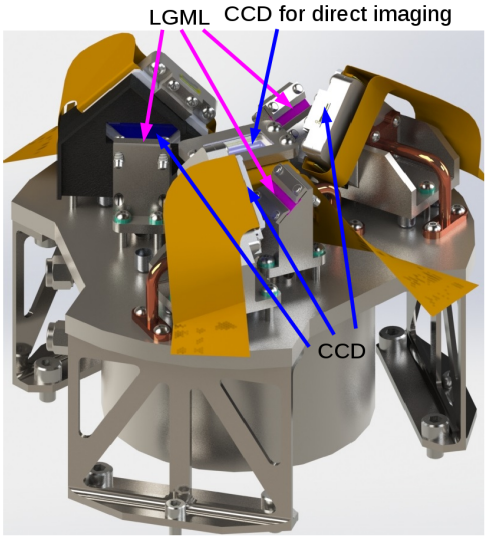

Fig. 13 Interior of the detector vacuum chamber showing almost all focal plane components: LGMLs, CCD faces, and flex prints (gold). A black anodized CCD baffle with a horizontal rectangular aperture restricts the view of the CCDs to its LGML. The cylinder at the base of the focal plane will be filled with liquid N_2 prior to launch in the sounding rocket implementation.

3.4 *Detectors*

The focal plane layout is shown in Fig. 13. For the CCD detectors, we use commercially available CCD cameras from XCAM. The CCDs are semicustom devices manufactured by e2v technologies. These CCDs have typical quantum efficiencies of 80% to 90% in the energy range of 150 to 500 eV. Each CCD has a 26.11- × 25.73-mm image area with 1632 horizontal and 1608 vertical active pixels and full frame readout. The small pixel size of 16 μm × 16 μm allows high-resolution imaging, but we can sum rows for fast readouts. Used with the spectrometer dispersion along the diagonal, the useful dispersion range is about 35 mm, giving a 35 to 75 Å (165 to 350 eV) bandpass.

3.5 *Background*

To estimate the particle background, we use results from the Suzaku satellite in low Earth orbit. For the REDSoX polarimeter, launching either from White Sands, Minnesota, or from Australia, the maximum altitude will be somewhat lower than Suzaku, so the Suzaku background will be taken as an upper limit. The particle background in the Suzaku backside-illuminated CCD was 5×10^{-8} cnt/s/keV/pixel or 1.5×10^{-5} cnt/s/mm^2 in a 0.2-keV band at 0.3 keV.[22] In the cross-dispersion direction, the dispersed spectral extraction region will be about twice the size of the optics HPD, about 60″ or 0.7-mm wide. In the dispersion direction, the spectra are 35-mm long. Using three detectors and exposing for 300 s yields 0.3 counts expected from particles. The x-ray background in the REDSoX polarimeter bandpass is dominated by galactic emission, about 10^{-3} cnt/s/(arcmin)^2 in the ROSAT C band or 540 ph/cm^2/s/sr/keV for ROSAT's area (220 cm^2) and bandwidth (0.1 keV).[23] Thus, we expect about 30 cnt in 300 s across the REDSoX polarimeter band in the solid angle of each detector. The LGMLs, however, have a bandpass of $\delta E = 0.025E$, giving <2 counts expected across the three detectors. Compared with a source with 50 to 1000 counts, these backgrounds are negligible. To avoid solar scattered background, we require that the angle between the telescope's line of sight and the Sun should be >120 deg, as demonstrated by ROSAT.[23]

3.6 *Baseline Performance*

For a polarimeter, a figure of merit is the MDP at 99% confidence, given as a fraction $\mathrm{MDP} = 4.29\sqrt{(R+B)/T}/(\mu R)$, where R is the source count rate, B is the background count rate in a region that is the size of a typical image, T is the observation time, and μ is the modulation factor of the signal relative to the average signal for a source that is 100% polarized.[4,24] For most polarimeters operating in the 2- to 8-keV band, the modulations factors peak at 0.5 to 0.7 [e.g., 3], whereas for the REDSoX polarimeter and other polarimeters based on Bragg reflection, $\mu > 0.90$. In Sec. 4, we verify that μ is this high for the REDSoX polarimeter.

The effective area of the system was also validated using ray tracing developed for the REDSoX polarimeter project (see Sec. 4). The integrated area of the system, defined as $\mathcal{A} = \int A(\lambda)\mathrm{d}\lambda$ is 185 cm^2 Å. For a source with a flat spectrum, $R = I\mathcal{A}$, where I, one of the Stokes parameters, is the source flux in ph cm^{-2} s^{-1} Å^{-1}. The zeroth-order detector also provides a measurement of I, with $\mathcal{A}_0 = 488$ cm^2 but with a less definite energy band due to the CCD spectral resolution.

Briefly, we describe how to measure the Stokes Q and U parameters using just the polarimetry channel data, for the simple case of a flat input spectrum. In flight, the system would measure count rates in each of three channels, denoted by R_i, for $i = 1 \ldots 3$. For given values of I, Q, and U

$$R_i = \mathcal{A}(I + \mu Q c_i + \mu U s_i), \tag{17}$$

where μ is averaged over the bandpass, $c_i = \cos 2\theta_i$, $s_i = -\sin 2\theta_i$, and θ_i is the orientation of channel i's LGML with respect to the coordinate system defining Q and U. If we arrange the observation so that $\theta_1 = 0$, then $\theta_2 = 2\pi/3$ and $\theta_3 = 4\pi/3$ for three detectors at 120 deg to each other, and we can solve Eq. (17) for the Stokes parameters, obtaining

$$\begin{aligned} I &= (R_1 + R_2 + R_3)/(3\mathcal{A}) \\ Q &= (2R_1 - R_2 - R_3)/(3\ \mu A) \\ U &= (R_2 - R_3)/(3^{1/2}\ \mu A). \end{aligned} \tag{18}$$

If $\theta_1 \neq 0$, then an appropriate rotation by θ_1 will properly orient Q and U on the sky. The linear polarization fraction is $\Pi = (Q^2 + U^2)^{1/2}/I$, and the angle of the linear polarization is $\phi = \arctan Q/U$. (The electric vector position angle, often denoted EVPA, is usually defined as the angle to the east from north.) In practice, Eq. (17) will be somewhat more complicated by the dependence of I and μ on λ, so solving for Q and U will require a likelihood analysis of $R_i(\lambda)$ and a forward-folding methodology.[25]

4 Raytrace Validation

We use the MARXS ray-trace code, which can handle polarized x-rays.[26] Details of the raytrace design and implementation are provided elsewhere.[27] Here, we give a general overview of the components of the raytrace and how they have been used to verify the system performance and assess tolerances independently of analytic methods. Figure 14 shows how rays pass through the system.

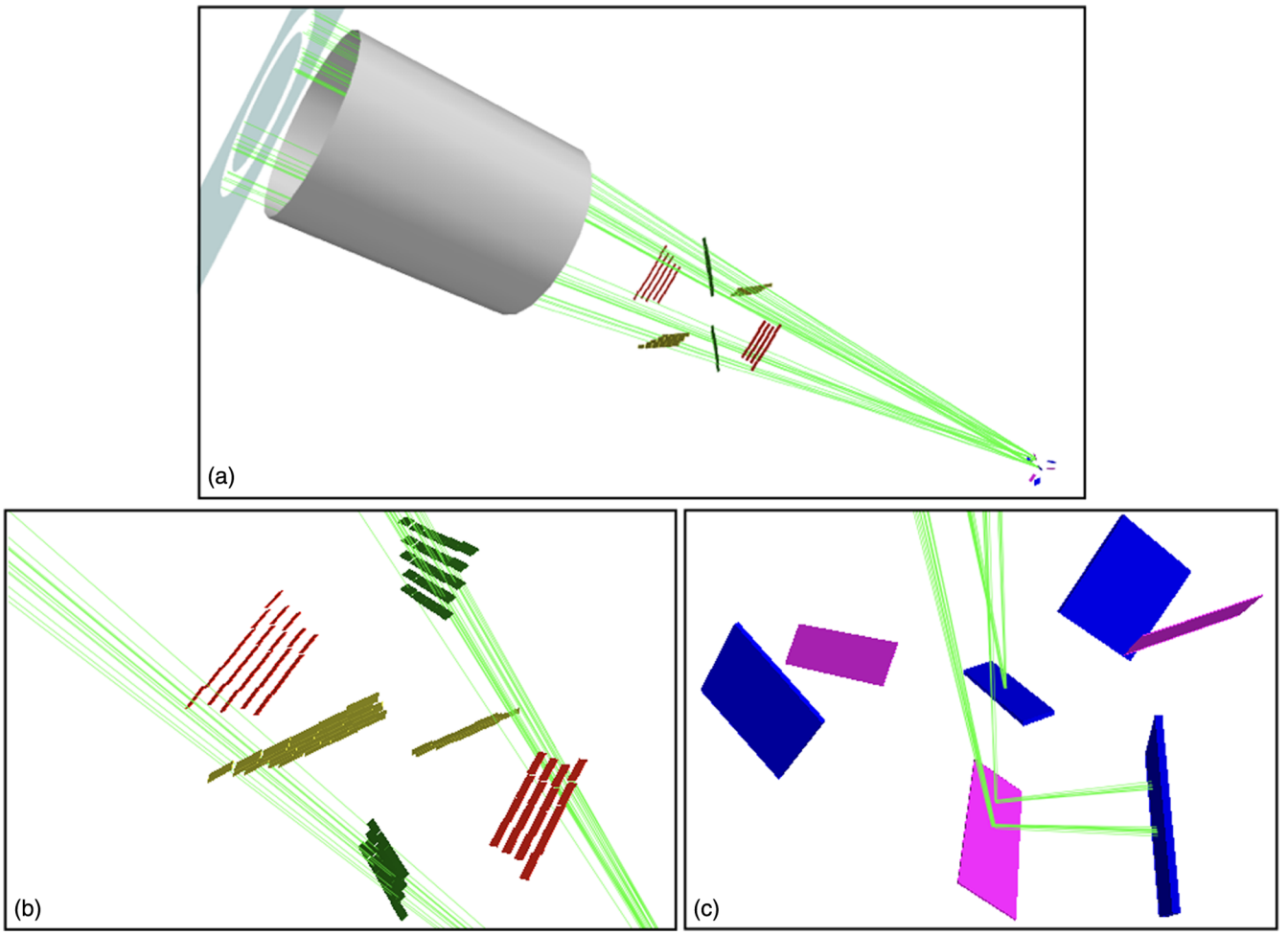

Fig. 14 Raytrace views of the REDSoX polarimeter. (a) and (b) The focusing mirror assembly is to the upper left and its output rays are green lines. Grating groups are paired (colored red, yellow, or green), with an upper group closer to the optics and a lower group closer to the focal plane. Rays of $E = 0.25$ keV going through only two opposing 60 deg (green grating) sectors are shown. (b) The view is limited to the grating facets. (c) Rays dispersed by the gratings (green) hit the corresponding LGML (magenta) before arriving at that channel's CCD (blue). Photons coming from the upper and lower grating groups in opposing sectors arrive at different positions along an LGML, where the Bragg condition is satisfied for rays incident at angles differing from 45 deg (see Sec. 3.2 for details). Some green lines represent zeroth-order photons going to the direct imaging CCD. Viewers can interact with this figure in the Supplemental Content using Adobe Acrobat. (3D Multimedia 2, PDF, 5.66 MB) [URL: http://dx.doi.org/10.1117/1.JATIS.4.1.011005.1].

The mirror was modeled with a simple thin lens approximation, with scattering that results in an HPD at the focus of 30″. The scattering was assumed to be Gaussian. Pointing jitter was included but has no effect on system performance until it exceeds 15″ at one sigma. The raytrace accounted for grating obscuration by the linear (L1) and hexagonal (L2) support structures (20% loss each) and realized grating efficiencies, based on synchrotron measurements.[19,20] The LGML reflectivities were taken from measurements shown in Fig. 12. The Bragg reflectivity to unpolarized light is well modeled as a Gaussian with an FWHM that is 2% of the wavelength at maximum. The reflectivity for *s*- and *p*-polarizations was obtained for a variety of wavelengths and angles around 45 deg using an on-line reflectivity calculator provided by the CXRO.[28] The CCD quantum efficiency is expected to be about 80%, based on lab data for comparable devices. The effective area and modulation factor as a function of wavelength are shown in Fig. 15.

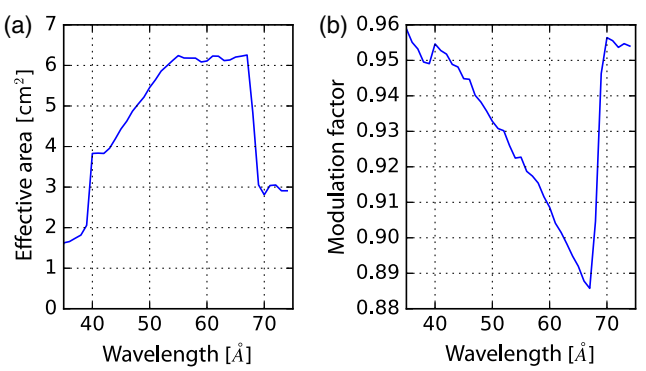

Fig. 15 (a) Effective area of our soft x-ray polarimeter design based on ray-tracing realistic components, as implemented in the REDSoX polarimeter. (b) Modulation factor based on the raytrace, averaging about 92% across the bandpass.

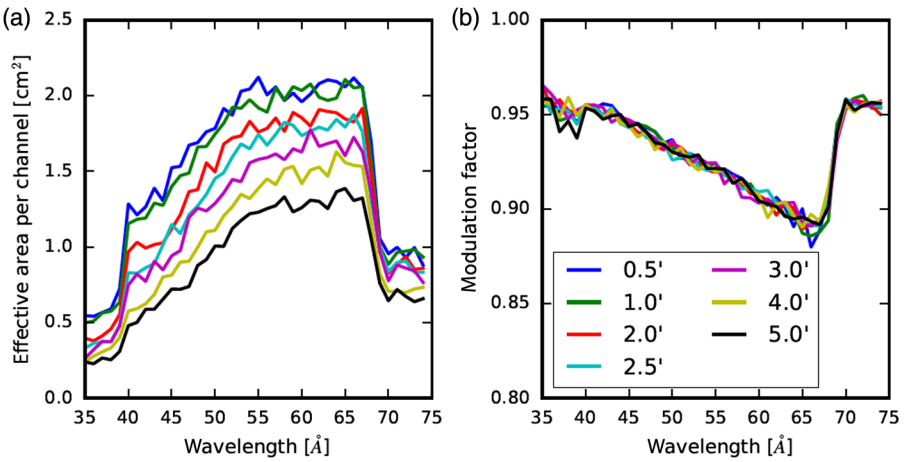

Fig. 16 Same as Fig. 15 except the focusing mirror's half-power diameter (HPD) was varied from 0.5′ to 5.0′. The mirror is expected to have an HPD better than 30″. The system is clearly robust to HPD degradation to as much as 60″ without significant effect on performance.

The raytrace was used to probe sensitivity to system design parameters that are not readily calculable. In Fig. 16, we show how the effective area and modulation factor change as the focusing mirror's HPD degrades from the nominal value of 30″. By restricting gratings to 60 deg sectors, mirror scatter contributes somewhat less to the spectral resolution than if full sectors were used. The breadth of the mirror's point response function is expected to have a full width at half maximum of about one-third that of the HPD, depending primarily on mirror shell alignment accuracy. As the HPD is varied, there is no obvious effect on the modulation factor, as the reflection angles off of the LGMLs change insignificantly. However, the effective area changes with the HPD as the spectral resolution degrades because photons are dispersed too far from the location on the LGML where Bragg reflectivity is maximized, i.e., the LGML's spectral resolution matches the grating spectrometer's spectral resolution until the HPD increases beyond 60″.

5 Science Objectives

Here, we describe potential scientific studies to be performed with an x-ray polarimetry mission with sensitivity in the soft x-ray band that would not be covered by instruments such as IXPE. Although the REDSoX polarimeter is limited to the 35 to 75 Å (165 to 350 eV) band due to limitations relating to implementation on a sounding rocket, LGML development could extend the bandpass to higher energies.

Blazars, which include BL Lac objects, high polarization quasars, and optically violent variables, contain parsec-scale jets with $\beta \equiv v/c \sim 0.995$ or higher. In the so-called high-synchrotron-peak blazars (HBLs such as Mk 421 and Mk 501), the x-ray spectrum is steeper than the optical spectrum, indicating that the x-rays are produced by synchrotron radiation from the highest energy electrons that are efficiently accelerated close to the base of the jet or at shock fronts farther downstream in the jet. For a differential electron energy distribution $n(E) \propto E^{-p}$, the maximum fractional polarization for synchrotron emission from relativistic electrons in a uniform B field is $P_{\max} = \frac{p+1}{p+7/3}$.[29] The spectral shape is a power law with energy index $\alpha = (p-1)/2$, so the photon indices are $\Gamma = (p+1)/2$ and $P_{\max} = \Gamma/(\Gamma + 2/3)$. For Mk 421, Γ is typically about 2.5 in the soft x-ray band, giving $P_{\max} = 0.79$, i.e., 79% polarized. Jet and shock models make different predictions regarding the direction of the magnetic field at x-ray energies. For knots in a laminar jet flow with cross-jet velocity gradients (as found in Mk 501[30]), it can be nearly parallel to the jet axis,[31] whereas for internal shocks it should be perpendicular.[32] Given the grasp of the system (Sec. 3.6), we expect about 5 counts/s from Mk 421. With $R \gg B$ (see Sec. 3.5), the MDP from a 300-s observation of Mk 421 will be 11%. As the x-ray spectrum of these blazars steepens with energy, we would expect the polarization fraction to increase with energy, so it would be extremely valuable to observe these targets simultaneously with IXPE.

Isolated NSs with strong magnetic fields are often very soft; they are too faint above 2 keV for IXPE but excellent targets for the REDSoX polarimeter. Our primary target for such an observation is RX J1856.4-3754, the brightest isolated NS in the ROSAT all sky catalog. A birefringence model of this source gave a prediction in the soft x-ray band of $\gtrsim$90% polarization,[33] validated by an optical polarization detection of 16%.[34] The MDP for the REDSoX polarimeter is 59%, sufficient to test the model. PSR B0656 + 14, a radio pulsar, is similarly x-ray bright and visible from the northern hemisphere. Here $X-1$, an accreting pulsar in a binary with an A star is another interesting target. The 50% pulsed soft x-ray emission could be nearly 100% polarized according to one model[35] or it could be more like 10% to 20%.[36] It is bright and has low N_H. We expect MDP = 20% using the REDSoX polarimeter, so these two models could be readily distinguished in an observation during a high state in its 35-day cycle.

An orbiting soft x-ray polarimeter (oSoX polarimeter) would obtain longer exposures and perhaps have larger area, so it would be capable of measuring the x-ray polarization of many other types of source, such as quasars and x-ray binaries (XRBs). X-ray emission from accretion onto black holes may arise from Compton scattering of thermal photons in a hot corona or from synchrotron emission or Comptonization by electrons in a highly relativistic pc-scale jet. Jets are frequently observed from such sources, so the x-rays should be polarized. In both cases, the origin of the jet is not resolved in the x-ray band, so x-ray polarization measurements can give an indication of the existence and orientation of jets within 10^3 gravitational radii.

Transient XRBs with stellar-mass black holes like XTE J1118 + 480 can be very soft and jets may contribute most of the x-rays[37]—confirmable using polarimetry. A jet model for XTE J1118 indicates that the soft x-ray polarization should be about 20%.[38] The source was discovered with XTE and detected by the extreme ultraviolet explorer at 100 eV, so the column density is well below 10^{20} cm^{-2}, making it a good target for the oSoX polarimeter. During its 2000 outburst, the flux density at 0.3 keV was brighter than Mk 421,[39] making it an excellent candidate for a target of opportunity observation.

Theoretical work indicates that AGN accretion disks and jets should be 10% to 20% polarized[6,40] and that the polarization angle and magnitude should change with energy in a way that depends on the system inclination and the black hole mass and spin. The variation of polarization with energy could be used as a probe of the black hole spin and the polarization position angle should rotate through 90 deg between 1 and 2 keV.[6] Thus, x-ray polarization measurements are needed both above 2 keV (e.g., with IXPE) and below 1 keV with the oSoX polarimeter.

Finally, Sy 2 galaxies exhibit polarized broad lines in optical spectra, an indication of scattering on a spatial scale much larger than the opaque torus that obscures the nucleus.[41] Similar scattering is expected in the x-ray spectrum below 1 keV, but there are many emission lines from photoexcited gas that are likely unpolarized.[42] The oSoX polarimeter would obtain a spectrum with sufficient resolution to separate lines and continuum to detect the scattered continuum or discern which lines originate closer to the nucleus and are scattered like the optical broad lines.

6 Summary

We have presented an arrangement of components that is specifically designed for soft x-ray polarimetry. We have been developing and testing potential components in the MIT polarimetry lab.[8–10,43] Although our proposed implementation is specifically targeted for use in a sounding rocket flight, the design should be readily adapted for orbital use. With exposure times of days to weeks, the MDP can easily be decreased to 1% or better, depending on the target. Many more types of sources may be observed in an orbital mission—cataclysmic variables, active galaxies, such as Seyfert 2 s, galactic black hole binaries, and possibly γ-ray bursts.

If the readout detector length can be increased by adding detectors, the bandpass and throughput of this design are then limited predominantly by the dispersion of the gratings and the efficiencies of the short-wavelength MLs. At higher dispersion, say with a longer focal length, the spectral resolution can be increased. For example, increasing the spectral resolution can be very useful for investigating the continuum between emission lines in Sy 2 galaxies.

We note also that the gratings are very thin and will pass high-energy x-rays, say $E > 3$ keV. This feature allows us to use this design in combination with a focal plane polarimeter to provide a wider energy range.

Acknowledgments

Support for this work was provided by the National Aeronautics and Space Administration through Grants NNX12AH12G and NNX17AE11G and by Research Investment Grants from the MIT Kavli Institute. The simulations make use of Astropy, a community-developed core Python package for astronomy.[44]

References

1. R. Novick et al., "Detection of x-ray polarization of the crab nebula," *Astrophys. J.* **174**, L1 (1972).
2. M. C. Weisskopf et al., "A precision measurement of the x-ray polarization of the crab nebula without pulsar contamination," *Astrophys. J.* **220**, L117–L121 (1978).
3. M. C. Weisskopf et al., "The imaging x-ray polarimetry explorer (IXPE)," *Proc. SPIE* **9905**, 990517 (2016).
4. P. Kaaret, "X-ray polarimetry," arXiv:1408.5899 (2014).
5. M. Chauvin et al., "Shedding new light on the crab with polarized x-rays," *Sci. Rep.* **7**, 7816 (2017).
6. J. D. Schnittman and J. H. Krolik, "X-ray polarization from accreting black holes: the thermal state," *Astrophys. J.* **701**, 1175–1187 (2009).
7. H. L. Marshall, "A soft x-ray polarimeter designed for broadband x-ray telescopes," *Proc. SPIE* **6688**, 66880Z (2007).
8. H. L. Marshall et al., "Progress toward a soft x-ray polarimeter," *Proc. SPIE* **8861**, 88611D (2013).
9. H. L. Marshall et al., "The use of laterally graded multilayer mirrors for soft x-ray polarimetry," *Proc. SPIE* **9144**, 91441K (2014).
10. H. L. Marshall et al., "The use of laterally graded multilayer mirrors for soft x-ray polarimetry," *Proc. SPIE* **9603**, 960319 (2015).
11. M. Born and E. Wolf, *Principles of Optics Electromagnetic Theory of Propagation, Interference and Diffraction of Light*, Pergamon Press, Oxford, United Kingdom (1980).
12. C. R. Canizares et al., "The Chandra high-energy transmission grating: design, fabrication, ground calibration, and 5 years in flight," *Publ. Astron. Soc. Pac.* **117**, 1144–1171 (2005).
13. H. L. Marshall et al., "The rocket demonstration of a soft x-ray polarimeter (REDSoX polarimeter)," *Proc. SPIE* **10399**, 103990K (2017).
14. O. Citterio et al., "Characteristics of the flight model optics for the JET-X telescope onboard the spectrum-x-gamma satellite," *Proc. SPIE* **2805**, 56–65 (1996).
15. G. Pareschi et al., "Development of grazing-incidence multilayer mirrors by direct Ni electroforming replication: a status report," *Proc. SPIE* **5900**, 590008 (2005).
16. B. D. Ramsey et al., "The development of hard x-ray optics at MSFC," *Proc. SPIE* **5168**, 129–135 (2004).
17. E. Figueroa-Feliciano et al., "Update on the micro-X sounding rocket payload," *Proc. SPIE* **8443**, 84431B (2012).
18. R. K. Heilmann et al., "Development of a critical-angle transmission grating spectrometer for the international x-ray observatory," *Proc. SPIE* **7437**, 74370G (2009).
19. R. K. Heilmann, A. R. Bruccoleri, and M. L. Schattenburg, "High-efficiency blazed transmission gratings for high-resolution soft x-ray spectroscopy," *Proc. SPIE* **9603**, 960314 (2015).
20. R. K. Heilmann et al., "Critical-angle transmission grating technology development for high resolving power soft x-ray spectrometers on Arcus and Lynx," *Proc. SPIE* **10399**, 1039914 (2017).
21. R. K. Heilmann et al., "Diffraction efficiency of 200-nm-period critical-angle transmission gratings in the soft x-ray and extreme ultraviolet wavelength bands," *Appl. Opt.* **50**, 1364 (2011).
22. B. LaMarr et al., "Front- and back-illuminated x-ray CCD performance in low- and high-earth orbit: performance trends of Suzaku XIS and Chandra ACIS detectors," *Proc. SPIE* **7011**, 70112C (2008).
23. S. L. Snowden et al., "ROSAT survey diffuse x-ray background maps. II," *Astrophys. J.* **485**, 125–135 (1997).
24. M. C. Weisskopf et al., "X-ray polarimetry and its potential use for understanding neutron stars," in *Neutron Stars and Pulsars*, W. Becker, Ed., Astrophysics and Space Science Library, Vol. **357**, p. 589, Springer, Berlin, Heidelberg (2009).
25. T. E. Strohmayer, "X-ray spectro-polarimetry with photoelectric polarimeters," *Astrophys. J.* **838**, 72 (2017).
26. H. M. Günther, J. Frost, and A. Theriault-Shay, "MARXS: a modular software to ray-trace x-ray instrumentation," *Astron. J.* **154**, 243 (2017).
27. H. M. Günther et al., "REDSoX: Monte-Carlo ray-tracing for a soft x-ray spectroscopy polarimeter," *Proc. SPIE* **10399**, 1039917 (2017).
28. E. Gullikson, "Multilayer reflectivity," 2010, http://henke.lbl.gov/optical_constants/multi2.html.
29. V. L. Ginzburg and S. I. Syrovatskii, "Cosmic magnetobremsstrahlung (synchrotron radiation)," *Ann. Rev. Astron. Astrophys.* **3**, 297 (1965).

30. M. Giroletti et al., "Parsec-scale properties of markarian 501," *Astrophys. J.* **600**, 127–140 (2004).
31. A. P. Marscher, "Relativistic jets and the continuum emission in QSOs," *Astrophys. J.* **235**, 386–391 (1980).
32. A. P. Marscher and W. K. Gear, "Models for high-frequency radio outbursts in extragalactic sources, with application to the early 1983 millimeter-to-infrared flare of 3C 273," *Astrophys. J.* **298**, 114–127 (1985).
33. D. González Caniulef et al., "Polarized thermal emission from x-ray dim isolated neutron stars: the case of RX J1856.5-3754," *Mon. Not. R. Astron. Soc.* **459**, 3585–3595 (2016).
34. R. P. Mignani et al., "Evidence for vacuum birefringence from the first optical-polarimetry measurement of the isolated neutron star RX J1856.5-3754," *Mon. Not. R. Astron. Soc.* **465**, 492–500 (2016).
35. T. Kii, "X-ray polarizations from accreting strongly magnetized neutron stars—case studies for the x-ray pulsars 4U 1626-67 and Hercules X-1," *Publ. Astron. Soc. Jpn.* **39**, 781–800 (1987).
36. J. Heyl and I. Caiazzo, 2018, "Strongly magnetized sources: QED and x-ray polarization," Galaxies special issue, The Bright Future of Astronomical X-ray Polarimetry, submitted.
37. S. Markoff, H. Falcke, and R. Fender, "A jet model for the broadband spectrum of XTE J1118+480. Synchrotron emission from radio to x-rays in the low/hard spectral state," *Astron. Astrophys.* **372**, L25–L28 (2001).
38. F. L. Vieyro, G. E. Romero, and S. Chaty, "Modeling the polarization of high-energy radiation from accreting black holes. A case study of XTE J1118+480," *Astron. Astrophys.* **587**, A63 (2016).
39. J. E. McClintock et al., "Complete and simultaneous spectral observations of the black hole x-ray nova XTE J1118+480," *Astrophys. J.* **555**, 477–482 (2001).
40. A. L. McNamara, Z. Kuncic, and K. Wu, "X-ray polarization in relativistic jets," *Mon. Not. R. Astron. Soc.* **395**, 1507–1514 (2009).
41. R. R. J. Antonucci and J. S. Miller, "Spectropolarimetry and the nature of NGC 1068," *Astrophys. J.* **297**, 621–632 (1985).
42. P. M. Ogle et al., "Testing the Seyfert unification theory: Chandra HETGS observations of NGC 1068," *Astron. Astrophys.* **402**, 849–864 (2003).
43. S. N. T. Heine et al., "Laboratory progress in soft x-ray polarimetry," *Proc. SPIE* **10399**, 1039916 (2017).
44. Astropy Collaboration et al., "Astropy: a community python package for astronomy," *Astron. Astrophys.* **558**, A33 (2013).

Herman L. Marshall is a principal research physicist at the Massachusetts Institute of Technology Kavli Institute. He received his SB in physics at MIT in 1978 and his PhD in astronomy at Harvard in 1983. He is the calibration scientist for the High Energy Transmission Grating Spectrometer on the Chandra X-ray Observatory, a coinvestigator on NASA's Imaging X-ray Polarization Explorer, and a principal investigator of the MIT X-ray Polarimetry Laboratory.

Biographies for the other authors are not available.